RSC Advances

REVIEW

View Article Online
View Journal | View Issue

Cite this: *RSC Adv.*, 2023, **13**, 31738

Recent advances in dynamic dual mode systems for daytime radiative cooling and solar heating

Shiqing Zhou, Pengyue Chen, Chunhong Xiao, Yuqing Ge and Hongwen Gao *

Thermal management, including heating and cooling, plays an important role in human productive activities and daily life. Nevertheless, in the actual environment, almost all the ambient scenarios come with the challenge that the objects are located in a quite dynamic and variable environment, which includes fluctuations in aspects such as space, time, sunlight, season, and temperature. It is imperative to develop low-energy or even zero-energy thermal-management technologies with renewable and clean energy. In this review, we summarised the latest technological advances and the prospects in this burgeoning field. First, we present the fundamental principles of the daytime passive radiative cooling (PDRC) thermal management device. Next, In the domain of dual-mode systems, they are classified into various types based on the diverse mechanisms of transitioning between cooling and heating states, including electrical responsive, mechanical responsive, temperature responsive, and solution responsive. Furthermore, we conducted an in-depth analysis of the principles and design methodologies associated with these categories, followed by a comparative assessment of their performance in radiative cooling and solar heating applications. Finally, this review presents the challenges and opportunities of dynamic dual mode thermal management, while also identifying future directions.

Received 13th August 2023
Accepted 24th October 2023

DOI: 10.1039/d3ra05506j

rsc.li/rsc-advances

1. Introduction

The greenhouse effect is a pressing issue exacerbated by rising carbon dioxide emissions,[1–5] population growth, and science and technological advancements. The escalating demand for traditional cooling technologies, such as air conditioning, particularly in hot and humid climates, has resulted in a noteworthy increase in energy consumption.[6] Furthermore, the heating, ventilating, and air conditioning load of the world is projected to rise by 6.2% per year.[7] In light of this trend, the significance of excellent energy saving technologies becomes more apparent. These technologies wield a substantial influence on the energy conservation of heating, ventilation, and air conditioning systems, which collectively account for 40% of the total energy consumption in buildings.[8]

Considering the above mentioned background, radiative cooling technology emerges as a critical player in waste heat treatment and conversion. Its eco-friendliness, and passive operation with zero-energy consumption contribute to sustainability.[9–11] These advantages reduce fossil fuel combustion and pollutant emissions. Importantly, radiative cooling is not subject to external control.[12–14] Numerical predictions suggest that this zero-energy heat management device has significant global, year-round energy saving potential, offering a viable path to net-zero carbon by 2050. Daytime passive radiative cooling technology can achieve cooling effect by utilizing material surfaces to reflect sunlight and simultaneously dissipate heat or thermal radiation to the cold universe ($\approx$3 K) through the atmospheric transparency window of 8 to 13 μm. It is featured with zero energy consumption and zero environmental pollution,[15–17] bringing about significant improvement compared with conventional cooling systems. Radiative cooling materials are often engineered to operate at elevated temperatures. This is achieved by adjusting materials that have high reflectance and high emissivity in long-wave infrared (LWIR) wavelengths. However, cooling is typically required only during hot seasons, and continuous PDRC may lead to excessive cooling during winter and nighttime. Therefore, the pursuit of dynamic PDRC, capable of adjusting cooling during hot weather and providing warmth in colder conditions, is essential and promising.

Typically, dynamic dual mode radiative cooling and heating systems are primarily achieved through a combination of smart materials or dynamic structures. This heating approach includes solar heating or radiative heating. However, not all materials possess the ability of radiative heating. Considering the practical convenience and zero energy consumption, solar heating is more widely adopted. Therefore, in this review, we mainly focus on solar heating.

In practical environments, the effectiveness of radiative cooling and solar heating faces challenges in nearly all

College of Environmental Science and Engineering, Tongji University, 1239 Siping Road, Shanghai 200092, P. R. China. E-mail: sqzhou@tongji.edu.cn; chen_pengyue@tongji.edu.cn; xiaochunhong@tongji.edu.cn; geyuqing@tongji.edu.cn; hwgao@tongji.edu.cn

scenarios. This is because objects are situated within highly dynamic and variable surroundings, encompassing spatial, temporal, sunlight, and seasonal changes, as well as fluctuations in temperature. The complexity of these environmental factors necessitates in-depth research and understanding to better adapt to and address the various challenges.

For practical applications, an efficient thermal management system is required to switch to the appropriate mode in response to dynamic environments.[18–20] Stimulus-responsive systems can be broadly categorized based on the source of the stimulus:[21–25] (a) chemical stimuli, (b) physical stimuli, or (c) biochemical stimuli in the solid-state, solution, or gel. The primary application scenarios for PDRC, include buildings,[26–28] windows,[29–31] solar cell cooling,[32–34] personal thermal management,[35–37] and water harvesting.[38–40] Physical stimuli, such as voltage[41,42] temperature changes,[43] light irradiation,[44] and mechanical strain play a crucial and promising role in developing intelligent response systems for PDRC.[45]

In recent years, numerous stimulus-responsive intelligent PDRC systems have sparked significant interest due to their versatile property.[46–48] It is well known that the dynamic dual-mode thermal management based on radiative cooling and solar heating holds the potential to significantly reduce the ever-increasing energy consumption. This has ignited a strong interest among researchers. Therefore, to promote real-world applications as well as further research and development in dynamic dual mode system, recent advances in dynamic dual mode systems for radiative cooling and solar heating were classified and summarized in this review.

First, the fundamental physics and thermodynamic concepts of PDRC are introduced, alongside the underlying theories of radiative cooling technologies. Meanwhile, we provide the evaluation parameters that can be potentially used for different types of dynamic dual mode systems. Further, we classified dynamic dual mode systems by switching stimuli categories and introduce their principles, characteristics, and progress. Finally, current research state of dynamic dual mode systems for radiative cooling and solar heating, and technical challenges and potential advancements are outlined.

2. Fundamentals of the daytime radiative cooling system

Daytime radiative cooling is a fascinating natural phenomenon that exploits the principle of cooling objects by radiating heat toward the night sky and outer space. At any temperature above absolute zero (0 K), objects spontaneously emit and absorb electromagnetic waves, resulting in heat exchange between objects at different temperatures. The radiative heat exchange between the Earth and outer space plays a crucial role in maintaining the Earth's viable temperature range.

The Earth's atmosphere has a unique transparency window in the wavelength range of 8 to 13 μm (Fig. 1a), known as the atmospheric window. This window allows thermal radiation to pass through the atmosphere, enabling

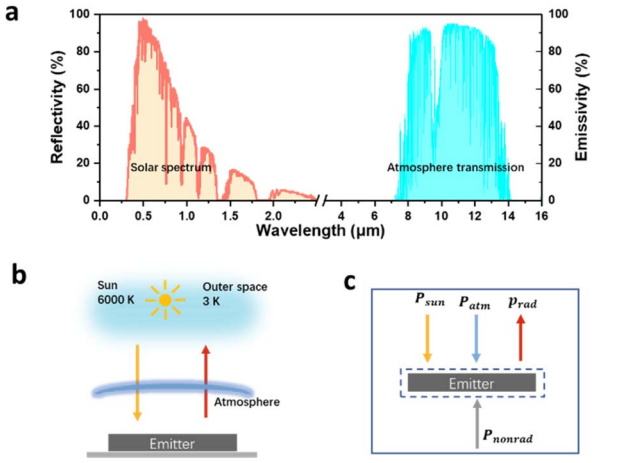

Fig. 1 (a) Solar spectrum (red shaded area) and the atmosphere transmission spectrum in the mid-infrared wavelength range (blue shaded area). (b) Thermal balance of daytime radiative cooling. (c) Radiative heat exchange process of daytime radiative cooling.

radiative sky cooling to occur.[49] Even if we have an ideally selective emitter that only emits within the atmospheric transparency window, it's still necessary to reflect more than 90% of incident sunlight to remain at ambient temperature.[50] In practice, it is necessary to reflect over 94% of sunlight to achieve meaningful daytime radiative cooling, particularly when considering the variations in atmospheric conditions across different geographic regions.[51] This is significant challenge when combined to emit strongly and selectively in the atmospheric window. To achieve efficient passive radiative cooling,[52–54] specific optical properties are required to maximize radiative heat transfer toward outer space in the atmospheric window while minimizing the absorption of solar heat within the 0.3 to 2.5 μm range.

3. Principle of the PDRC system

3.1 The average reflectance ($\bar{R}_{solar}$)

$\bar{R}_{solar}$ within the solar irradiation 0.3 to 2.5 μm can be expressed as:

$$\overline{R}_{solar} = \frac{\int_{0.3}^{2.5} I_{solar}(\lambda)\rho(\lambda)d\lambda}{\int_{0.3}^{2.5} I_{solar}(\lambda)d\lambda} \quad (1)$$

where the symbol λ represents the wavelength, $I_{solar}(\lambda)$ is the solar radiation intensity of the standard AM1.5 spectrum, and $\rho(\lambda)$ refers to the solar reflectance of the sample.

3.2 The average emissivity ($\bar{\varepsilon}_{LWIR}$)

$\bar{\varepsilon}_{LWIR}$ within can be expressed as:

$$\bar{\varepsilon}_{LWIR} = \frac{\int_{8}^{13} I_{BB}(T_S\lambda)\varepsilon(\lambda,\theta)d\lambda}{\int_{8}^{13} I_{BB}(T_S\lambda)d\lambda} \quad (2)$$

where $I_{BB}(\lambda,\theta)$ represents the spectral intensity emitted by a standard blackbody with temperature and ε is the spectral emissivity of an emitter.

$$I_{bb}(T_S\lambda) = \frac{1}{\int_8^{13} I_{bb}(T_S\lambda)d\lambda} \quad (3)$$

3.3 Cooling power

Cooling power is a crucial parameter for evaluating the performance of PDRC. Several factors influence cooling power, including absorbed solar radiation, external thermal radiation, solar reflection, downward atmospheric thermal radiation, and non-radiative heat transfer, as depicted in Fig. 1b. Absorbed solar radiation predominantly occurs during the day within the wavelength range of 0.3 to 2.5 μm. On the other hand, external thermal radiation primarily takes place within the range of 2.5 to 25 μm. The downward atmospheric thermal radiation mainly comprises contributions from gas molecules and aerosol particles. Additionally, non-radiative heat transfer power involves heat conduction and convective energy losses between the PDRC surface and the surrounding environment.

$$P_{net} = P_{rad} - P_{atm} - P_{sun} - P_{nonrad} \quad (4)$$

In this equation,[43] P_{net} is the net cooling power (Fig. 1c). P_{rad} is the radiative power of the radiative body. P_{atm} and P_{sun} represents the power absorbed from atmospheric radiation and solar radiation,[55] respectively. P_{nonrad} is the total power loss due to all non-radiative heat transfer processes (such as convection and heat conduction between the radiative body and the surrounding environment).

$$P_{rad}(T_E) = A\int \cos\theta\, d\Omega \int_0^{\infty} I_{BB}(T_E\lambda)\varepsilon(\lambda,\theta) \quad (5)$$

In this context, $I_{BB}(T_E,\lambda)$ represents the spectral radiance of a blackbody at a temperature T_E. Ω denotes the solid angle. θ signifies the angle between the direction of the solid angle and the normal direction of the radiating body's surface. T_E and A refer to the temperature and area of the radiating body, respectively.

$$P_{atm}(T_{amb}) = A\int \cos\theta\, d\Omega \int_0^{\infty} I_{BB}(T_{amb}\lambda)\varepsilon(\lambda,\theta)\varepsilon_{atm}(\lambda,\theta) \quad (6)$$

In this equation,[56] $\varepsilon_{atm}(\lambda,\theta) = 1 - t(\lambda)1/\cos\theta$, where $t(\lambda)$ represents the atmospheric transmittance in the zenith direction. ε refers to the emissivity (absorptivity) of the radiating body, ε_{atm} denotes the atmospheric emissivity, and T_{amb} stands for the ambient temperature.

$$P_{sun}(T_E) = A\theta_{sun}\int_0^{\infty} d\lambda\, I_{AM1.5}(\lambda)\varepsilon(\lambda,\theta_{sun}) \quad (7)$$

where θ_{sun} represents the angle between the direction of solar radiation incidence and the normal direction of the surface. $\varepsilon(\lambda,\theta_{sun})$ is the average emissivity of the radiating body at wavelength λ and angle θ.

$$P_{nonrad} = Ah_c(T_{amb} - T_c) \quad (8)$$

where the symbol h_c represents the overall heat transfer coefficient, considering both convection and conduction heat transfer between the environment and the radiating body.

3.4 Temperature drop ΔT

$$\Delta T = T_{amb} - T \quad (9)$$

where, T_{amb} represents the ambient temperature, while T refers to the temperature of the PDRC material. The temperature reduction refers to the actual temperature decrease achieved by the material during the radiative cooling process. The temperature reduction can be measured experimentally, such as by monitoring the surface temperature of the material using thermocouples in real-world application environments.

4. Evaluation parameters for dual mode system

Intelligent radiative cooling materials respond adaptively to environmental conditions and demands. Their performance parameters include traditional radiative cooling material metrics as well as characteristics related to intelligent response.[57–59] Evaluating these combined parameters offers comprehensive insights into the materials' efficiency in achieving optimal radiative cooling. However, owing to the distinct stimulus factors associated with each type of intelligent PDRC material, their respective evaluation criteria also vary. We summarized the commonly used evaluation parameters as follows.

4.1 Switching response time

The switching response time is a critical parameter that characterizes the dynamic behavior of multimodal intelligent radiative cooling materials in adapting to changing environmental conditions. It quantifies the time required for the material to achieve a new equilibrium state after being subjected to modifications in its surroundings. The measurement of the switching response time involves monitoring the rate of change in the material's optical properties under different environmental stimuli, enabling a comprehensive assessment of its responsiveness and adaptability.

4.2 Response threshold

The response triggering threshold denotes the specific environmental conditions, such as temperature or humidity levels, at which the material initiates observable changes in its optical properties. This critical parameter establishes the minimum stimulus magnitude required to elicit a detectable response from the material, providing valuable insights into its sensitivity and responsiveness to external factors.

4.3 Reversibility

Reversibility pertains to the material's ability to maintain stability and repeatability in its optical property changes across multiple response cycles. This crucial characteristic is assessed by subjecting the material to cyclic testing under diverse environmental conditions and observing the consistency of its optical property variations over successive cycles. A high level of reversibility implies a robust and reliable performance, making it an essential aspect to consider in evaluating the suitability and durability of the material for practical applications.

4.4 Reflectance modulation, emissivity modulation (ΔR, $\Delta\varepsilon$)

In intelligent radiative cooling systems, it is crucial for the materials to regulate both reflectance and emissivity is crucial. The reflectance modulation degree quantifies changes in the material's reflectance within the solar spectrum range under varying environmental conditions, calculated as the difference between maximum (R_{max}) and minimum (R_{min}) reflectance values observed in specific environmental scenarios. By measuring reflectance under diverse conditions, the material's responsiveness to external factors and effectiveness in controlling solar radiation can be evaluated.

Similarly, the emissivity modulation degree characterizes variations in the material's emissivity within the infrared spectrum under diverse environmental conditions. It is determined by calculating the difference between maximum (ε_{max}) and minimum (ε_{min}) emissivity values observed under specific environmental settings. Measuring emissivity under different conditions provides valuable insights into the material's responsiveness to thermal radiation, contributing to its potential for effective radiative cooling applications. The detailed formulae are as follows:

$$\Delta R = R_{max} - R_{min} \quad (10)$$

$$\Delta\varepsilon = \varepsilon_{max} - \varepsilon_{min} \quad (11)$$

4.5 Net cooling power modulation, ΔP_{net}

The cooling power modulation degree signifies the extent of variations in the material's cooling performance under diverse environmental conditions. This critical parameter is calculated by measuring the cooling power of the material across different environmental scenarios, employing the formula:

$$\Delta P_{net} = P_{net,max} - P_{net,min} \quad (12)$$

where $P_{net,max}$ represents the maximum cooling power of the material observed under a specific environmental condition, and $P_{net,min}$ represents the minimum cooling power of the material observed under another specific environmental condition.

5. Intelligent responsive dual mode for radiative cooling and solar heating

5.1 Electro-responsive dual mode system

Electrochromic materials can reversibly change their transmittance or reflectance in the visible and infrared light range under external electrical or electrochemical stimulation.[60,61] To effectively regulate optical properties, electrochromic materials are typically assembled into electrochromic devices,[62,63] which can operate in either transmissive or reflective modes. A typical electrochromic device includes two transparent conductive layers (Fig. 2), an ion transport layer, an ion storage layer, and an electrochromic layer. Under the action of an external electric field, charge transfer occurs on the electrochromic layer, thereby realizing the electrochromic phenomenon. Based on material types, electrochromic materials can be divided into inorganic electrochromic materials and organic electrochromic materials.

Indeed, inorganic electrochromic materials are esteemed for their superior stability, remarkable durability, and high reflectance, making them highly suitable for extensive applications in various fields. Conversely, organic electrochromic materials, encompassing conductive polymers, organic small molecules, and triphenylamine-based polymers, demonstrate reversible optical modulation mechanisms involving polariton generation and redox elimination. These organic materials offer notable advantages, including elevated contrast ratios, versatile multicolor capability, and rapid response times.

As the best-known electrochromic material, WO_3 exhibits reversible oxidation–reduction reaction driven by specific chemical processes,[64,65] showing blue color upon ion and electron insertion and becoming transparent upon extraction. The specific electrochromic reaction equation of WO_3 can be described as follows:[66]

$$WO_3\ (\text{bleached}) + xM^+ + xe^- = 4M_xWO_3\ (\text{colored})$$

where M can be H, Li, Na, or K, and e^- represents an electron. Along with the dual injection and extraction of ions and electrons, the emissivity of WO_3 can also be reversibly changed.

Mandal *et al.* reported the broadband electrochromic performance of $Li_4Ti_5O_{12}$ from visible to IR regions,[67] significantly extending its application. With the intercalation of Li^+,

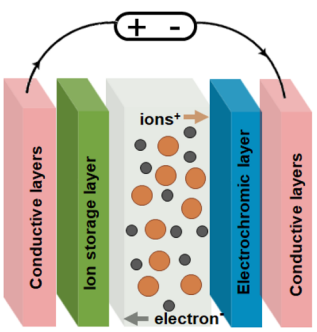

Fig. 2 Schematic of electrochromic device.

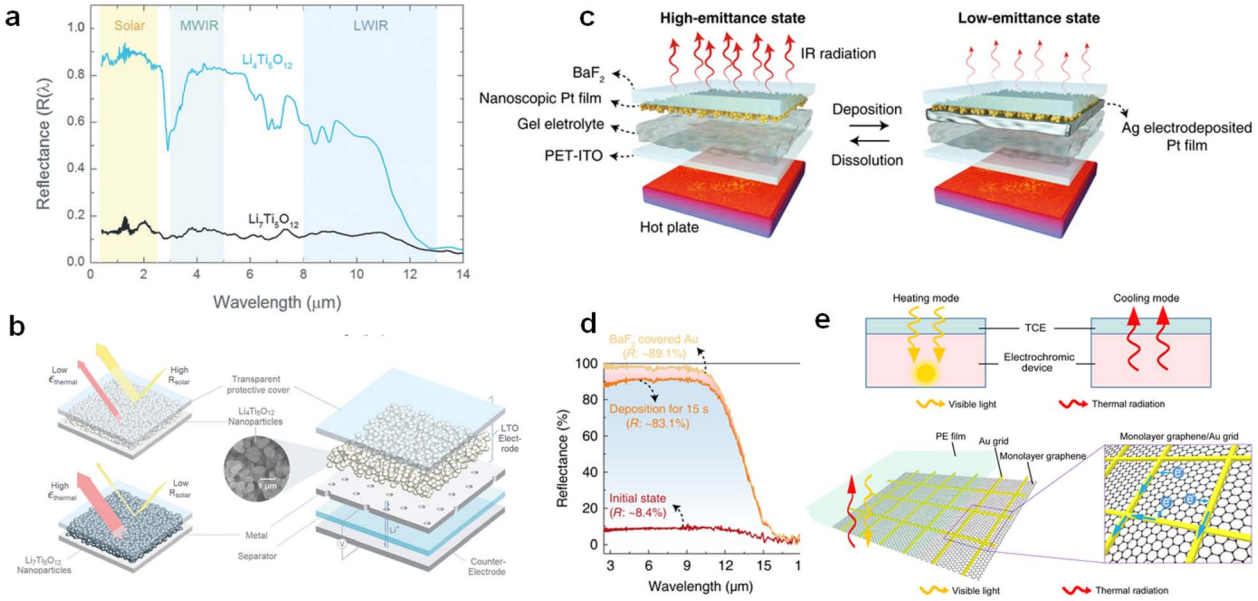

Fig. 3 (a) Visible-to-infrared spectral reflectance R of $Li_4Ti_5O_{12}$ and $Li_7Ti_5O_{12}$ nanoparticles deposited on Al foil and covered by barium fluoride (BaF_2). (b) Left is super-broadband emittance and reflectance, right is schematic of an electrochemical cell containing an "outward-facing" $Li_4Ti_5O_{12}$-based electrode. (c) Schematics of a nanoscopic Pt film-based RSE device (left) before and (right) after electrodeposition. (d) Total IR reflectance spectra of the 3 nm Pt/BaF_2 substrate before and after Ag electrodeposition (15 s) in an RSE three-electrode system. (e) To switch between solar heating and radiative cooling, the TCE must be transparent to both solar and mid-IR radiation while being highly conductive. Below is schematic of the proposed ultra-wideband transparent conducting electrode. The monolayer graphene provides uniform local conductance for charge transport, and the gold microgrid is responsible for long-range conductance with only minimal shadow loss of transmittance. (a and b) These figures have been adapted from ref. 63 with permission from Mandal, copyright 2023. (c and d) These figures have been adapted from ref. 64 with permission from Li, copyright 2020. (e) This figure has been adapted from ref. 65 with permission from Rao, copyright 2021.

$Li_4Ti_5O_{12}$ changed from delithiated state ($Li_4Ti_5O_{12}$, wide bandgap semiconductor state) to lithiated state ($Li_7Ti_5O_{12}$, metal state) (Fig. 3a and b). The high optical tunability in the solar region, mid wave IR region, and long wave IR region were 0.74, 0.68, and 0.30, achieving reversible radiative cooling and solar heating.

Metals can be easily colored by incorporating thin dielectric optical coatings owing to the high reflectance in the visible spectrum, providing possible visible coloring strategies without substantially affecting their IR properties. However, despite these advantages, systems that can fully use the properties of metals to attain dynamic IR modulation have not yet appeared. Li *et al.* reported reversible silver electrochemical deposition (RSE) devices based on nanoscopic platinum (Pt) films for adaptive thermal camouflage.[68] The nanoscopic Pt films exhibit high IR absorption and partial transmission (Fig. 3c and d), resulting in high-emittance states without metal deposition. With the application of a deposition voltage, silver (Ag) is electrodeposited on the Pt film surfaces, converting IR absorption and transmission to IR reflection and achieving low-emittance states. These devices can switch between high and low emittance states for multiple cycles. They demonstrate large and consistent IR tunability in both mid-wave IR (MWIR; 3 to 5 μm) and long-wave IR (LWIR, 7.5 to 13 μm) atmospheric transmission windows ($\Delta\varepsilon_{MWIR} = 0.77$, $\Delta\varepsilon_{LWIR} = 0.71$).

As shown in Fig. 3e, a flexible ultra-wideband transparent conducting electrode has been developed by Rao *et al.*,[69] enabling an electrochromic device with remarkable capabilities in synergistic solar and radiative heat management. The device can switch between solar heating mode ($R = 0.60$, $\varepsilon = 0.20$) and radiative cooling mode ($R = 0.33$, $\varepsilon = 0.94$) through optimal electrodeposition morphology.

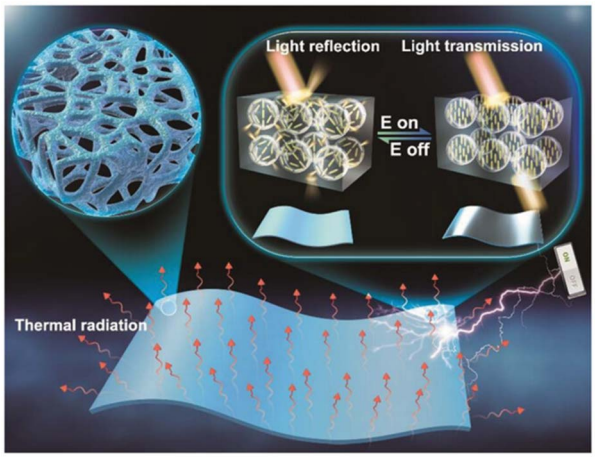

Fig. 4 Schematic illustration of the working principle of the PDRC polymer-dispersed liquid crystal film. This figure has been adapted from ref. 70 with permission from Deng, copyright 2023.

Another electro-responsive material that can be used in dual mode systems is electro-controlled polymer-dispersed liquid crystal. A polymer-dispersed liquid crystal-based PDRC smart window showing enhanced infrared emissivity within the wavelength of 8–13 μm was designed and prepared by Deng *et al.* (Fig. 4).[70] Obtained film is opaque and scatters iridescent light without an electric field because the randomly aligned directors of liquid crystal microdroplets cause a mismatch of refractive index between liquid crystal droplets and polymer matrix. Only a small amount of light could pass through the film. By applying voltage, liquid crystals are forced to uniformly align in the direction of the electric field, making the film transparent. In this case, most of the light could be transmitted inside. This dual mode system can be tuned in an on-demand and ultrafast millisecond-scale way.

5.2 Mechanically responsive dual mode system

Mechanical responsive materials exhibit tuneable optical properties upon the application of mechanical strain, enabling the modulation of reflectance or transmittance. Given the dependence of various scattering mechanisms on length scales, mechanical responsiveness is typically achieved by reconfiguring the surface morphology (two-dimensional scatterers) or internal structure (three-dimensional scatterers) of the material. Light scattering can be divided into three types through the relationship between the size of the scattering points and the wavelength of incident light based on dimensionless parameters χ, which is expressed as:

$$\chi = \frac{2\pi r}{\lambda} \tag{13}$$

where r is the radius of scattering point and λ is the wavelength of incident light. The value of χ represents three different types of light scattering. Light scattering is classified into three types based on χ: (1) $\chi \ll 1$ for Rayleigh scattering, (2) $\chi \approx 1$ for Mie scattering, and (3) $\chi \gg 1$ for geometric scattering.[69]

Common strategies include utilizing porous or nanoparticle composite materials and textiles, and introducing folds or layered buckling geometries. Mechanical responsiveness offers a simple approach to actively tuning optical properties with fast response times and good reversibility. Additionally, some mechanically responsive materials can be operated by straightforward manual manipulation, *e.g.* flipping between different surfaces of layers. Under elevated temperatures, the radiative cooling layer becomes exposed; conversely, under lower temperature conditions, the solar-absorbing layer is revealed. This approach is commonly employed in personal thermal management systems due to its simplicity for textiles.

5.2.1 Porous structure. The random boundaries of scattering structures present challenges in constructing a structural unit cell model for quantitative analysis. Moreover, a high core volume of the particles can lead to reduced transmittance in the initial transparent state, increased weight, decreased flexibility, and a limited number of scattering sites. To improve this, Cho *et al.* proposed a novel approach involving a 3D nanocomposite film with an ultrathin Al_2O_3 nano shell (approximately 60 nm) inserted between elastomers within a periodic 3D nanonetwork (Fig. 5a).[71] This innovative design enables the realization of high-performance mechano-responsive smart windows, and practical demonstrations have been conducted to validate its effectiveness.

Regardless of the stretching direction, numerous light-scattering nanogaps (corresponding to the porosity of up to 37.4 vol%) form at the interfaces of Al_2O_3 and the elastomers under stretching. This results in the gradual modulation of transmission from 90% to 16% at visible wavelengths and does not degrade with repeated stretching/releasing over more than 10 000 cycles. To validate the concept, a smart window device enabled by a mobile app for internet of things applications was created using the proposed 3D nanocomposite. This concept was successfully scaled up to the dimensions of 3 × 3 inches (Fig. 5b).

The loaded mechanical force can serve as a switch for a specially designed dual mode system, which helps to further enhance its solar heating performance. It is important to note that the heating performance is primarily governed by the amount of solar energy transmitted. By introducing an additional layer capable of enhancing solar absorption, the dual mode system could attain higher temperatures in cold weather than previously achievable. Zhao *et al.* utilized the above-mentioned strategy to craft porous structural composites.[72] They designed a bilayer material with a porous PDMS layer and an additional layer containing carbon black, intended for solar heating. Under pressure, the top layer can alternate between a transparent solid state for sunlight absorption and a highly porous state for solar reflection and radiative cooling (Fig. 5c). In its transparent state, this bilayer system absorbs nearly 95% of sunlight while reflecting about 93% of solar radiation in its porous state. It reflects approximately 94% of LWIR thermal emission in porous state, yielding a sub-ambient temperature reduction of roughly 5 °C in hot weather conditions (35 °C). It is a material system that achieves cooling and heating effects simultaneously in a truly practical manner. Li *et al.* obtained flexible thermoplastic polyurethane nanofiber (Es-TPU) membranes *via* electrospinning.[73] The Es-TPU can switched between radiative cooling and solar heating through changes in its optical reflectivity and emissivity by stretching. Es-TPU reached a reflectivity of 61.1% ($\Delta R = 34.5\%$) under an elongation strain of 80% (Fig. 5d and e). Consequently, this resulted in a net temperature increase of 9.5 °C above ambient in solar heating mode and a temperature drop of 10 °C at midday.

5.2.2 Wrinkles. Wrinkles are ubiquitous in our surroundings, ranging from creased clothing to wrinkles on the skin, with sizes spanning length scales from nanometers to meters. The wrinkle-based dynamic radiative response (DRR) mechanical system consists of two components: a thin film and a flexible substrate. Both components are optically transparent when in a flat state. Wrinkling is generated through a strain-release process. Specifically, a relatively stiff material is first deposited onto a pre-stretched elastomeric substrate. Upon the release of the pre-strain, wrinkles form due to the mismatch in moduli between the thin layer and the elastomeric substrate. The wrinkled surface refracts incident light in various

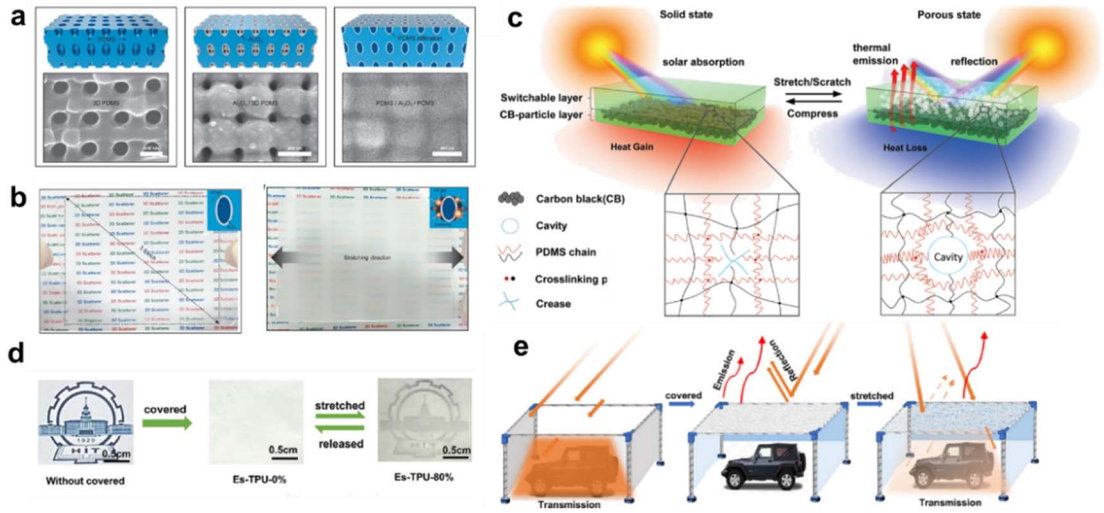

Fig. 5 (a) Digital photographs of the large-area 3D scatterer before stretching (transparent state) and (b) after stretching (opaque state). Inset: the air gap formation/recovery process in the 3D scatterer upon stretching/releasing. (c) Schematic of the bilayer structure consisting of a switchable silicone top layer and carbon black particle (CBP)-embedded bottom layer (SPDMS*x*–CBP film, where *x* is the water ratio used in film fabrication) and its cooling and heating mechanism. (d) Photographs of the substrates covered by nothing (left), Es-TPU-0% (middle), and Es-TPU-80% (right). (e) Schematic illustration of the optical regulation of Es-TPU membrane. (a and b) These figures have been adapted from ref. 67 with permission from Cho, copyright 2020. (c) This figure has been adapted from ref. 68 with permission from Zhao, copyright 2020. (d and e) These figures have been adapted from ref. 69 with permission from Li, copyright 2023.

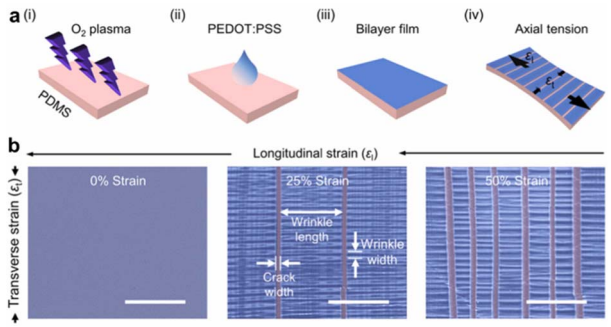

Fig. 6 Strain-dependent spectral modulation of a mechano-responsive dynamic window. (a) The schematic fabrication process of a bilayer film. The stretched bilayer film along the longitudinal direction (ε_l) caused transverse strain (ε_t) due to the Poisson effect. (b) SEM images of a bilayer film with different longitudinal strains. The tinted zone distinguished the cracks and wrinkles. Scale bars, 50 μm. (a and b) These figures have been adapted from ref. 67 with permission from Zhou, copyright 2022.

directions depending on the angle of incidence, reducing the optical transmittance. Once the bilayer structure is stretched back to the pre-strain level, the wrinkles disappear, and the film exhibits high transparency.

Zhou *et al.* applied a PEDOT:PSS coating on the surface of PDMS, as shown in Fig. 6a.[74] PDMS is the stiff substrate, and PEDOT:PSS is the soft layer which can have cracks. It is evident that the mismatch in elongation between PDMS (135%) and PEDOT:PSS (7.7%) leads to the formation of longitudinal cracks in PEDOT:PSS to release local stress (Fig. 6b). At low strain levels, the film exhibits high solar transmittance (80%) and high thermal reflectance (41%). Increasing the strain can dramatically reduce both the solar transmittance and thermal reflectance, reaching 16% and 50%, respectively, when the strain is as high as 25%. Compared to the released state, the stretched state shows a 55% reduction in solar transmittance and a 25% increase in thermal emissivity. In contrast to mechanically tuneable chromogenic windows that primarily operate in the solar spectrum, the proposed bilayer dynamic window demonstrates a broader spectral modulation from the solar spectrum to the mid-infrared region. Similarly, transverse wrinkles and longitudinal cracks can separately adjust the solar transmittance and thermal emissivity during the stretching process. The window can achieve rapid and reversible switching between the released heating mode and the stretched cooling mode, allowing the internal temperature of the housing model to be regulated by 4 °C.

5.2.3 Special structure design. Kirigami, the ancient art of paper folding and cutting techniques, has provided considerable inspiration for the design of material structure over the last few decades. The kirigami structure can transform a two-dimensional plane into a variety of three-dimensional structures independent of scales (Fig. 7a),[42] providing space for the preparation of structures with geometric gradients. The deformation of the kirigami structure will be enhanced with the increase of the external load (Fig. 7b). After removing the load, the kirigami structure can spontaneously return to the plane state. Such kind of performance of kirigami structure may bring some changes in optical property of design structures.

Wang *et al.* propose a novel dual-control smart window design consisting of 2 layers. The upper layer is PDMS-based kirigami structure with strain-responsive out-of-plane opening

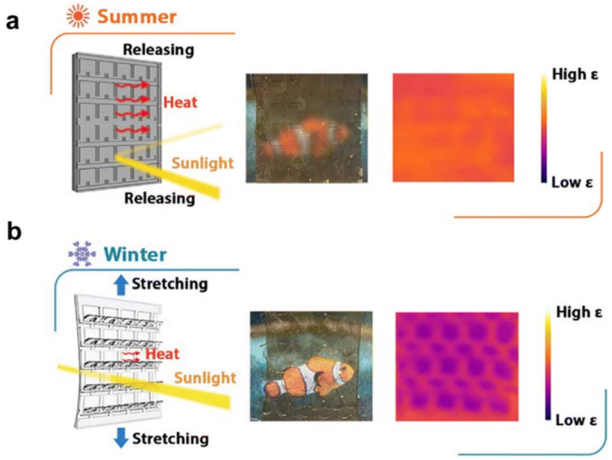

Fig. 7 (a) The working principle of the durable solar/radiative cooling (RC) dual-control smart window in summer and its corresponding photo and IR camera image. The red arrows represent thermal radiation and the yellow line represents sunlight. In summer, the high-ε kirigami overlayer closes to promote thermal radiation and the hydrogel turns translucent to block the sunlight. (b) The working principle of the durable solar/RC dual-control smart window in winter and its corresponding photo and IR camera image. In winter, the kirigami overlayer opens towards the outside environment under in-plane stretching, which allows sunlight to enter the room to suppress the RC to minimize heat loss. This figure has been adapted from ref. 42 with permission from Wang, copyright 2023.

for emissivity tuning.[75] The bottom layer used PDMS to laminate thermal-responsive composite hydrogels coated with Ag nanowires (AgNWs) based on physical-crosslinked poly(*N*-isopropylacrylamide) (pNIPAm). In summer, the thermochromic hydrogel turns translucent to suppress the solar heat gain. Furthermore, the high emissivity kirigami structure covers the exterior surface of the window, promoting radiative cooling. In winter, the hydrogel becomes transparent to allow for solar transmission. Additionally, the kirigami structure undergoes an out-of-plane structural change, opening towards the outside environment to expose the underlying low-emissivity silver nanowires and suppress heat radiation. Such design provides a promising solar transmittance modulation ability of 24% and a good long-wave infrared emissivity regulation ability of 0.5. Furthermore, its lifespan is nine times longer than conventional smart hydrogels.

5.2.4 Janus structure. The underlying principle of this approach is inherently straightforward: positioning the radiative cooling layer externally during elevated temperatures and, conversely, situating the solar absorption layer externally during lower temperatures. Typically, heating and cooling modes are often integrated into one substrate. The arrangement of these two modes can be either vertical (top and bottom) or horizontal (left and right). When they were in horizontal setups, electric assistance is often utilized,[76] while in vertical configurations, a straightforward flipping method is commonly employed.

Li *et al.* developed a dual mode thermal management device,[77] primarily comprising a pair of rotating actuators or rollers and a thin film polymer composite material (Fig. 8a–c). For cooling mode, Ag film is the electrode for exerting the electrostatic force (Maxwell pressure) and for reflecting the solar radiation. The top PDMS layer is visibly transparent and infrared-emissive for radiative cooling. For heating mode, Cu is the electrode for supplying static charge, and Cu/Zn is the plasmonic selective absorber. When a mode transition is necessitated due to weather or shifts in energy balance, the actuators pull the heating/cooling material along the track system, exposing the required section of the material in the desired mode, while the remaining material is rolled up and collected. Ly *et al.* fabricated a dual mode asymmetric Janus photonic mirror consisting of a silicon-based diffraction grating that achieves 20% IR modulation of both outgoing and incoming radiation (Fig. 8d).[78] The cooling mode permits broadband emission of thermal radiation from the vehicle and reflection of thermal radiation from the environment with an interior space temperature 8 °C lower than radiative cooling only in summer. The heating mode reverses the flow of heat through the thermal channel while raising the interior space temperature by 5.7 °C in winter.

Due to its minimal impact on the primary characteristics, large-scale production, and extended applications of textiles, the reversible Janus design finds broader and more practical applications within the thermal management of textile materials. Yang *et al.* utilized NaH_2PO_2 particles characterized by elevated infrared emissivity,[79] incorporated within a porous polymethyl methacrylate film (Fig. 9a). The unique refractive indices, coupled with the porous structure and NaH_2PO_2 particles, synergistically enhance the overall scattering efficiency, culminating in the establishment of a markedly reflective interface. The heating aspect is comprised of densely packed cotton fibers featuring surface-incorporated polypyrrole, thereby demonstrating a commendable performance in photothermal conversion. In an outdoor environment under 750 mW cm^{-2} solar radiation, the sub-ambient cooling temperature of the dual mode Janus film is 8.8 °C, while the heating temperature reaches 39.3 °C, indicating excellent thermal management capabilities.

Xiang *et al.* employed electro spun PVDF-HFP as the cooling layer,[80] with the heating layer introduced onto the PVDF-HFP membrane through a straightforward spray deposition method (Fig. 9b). Feng *et al.* proposed a Janus-type nanofabric. Hollow TiO_2 particles were introduced in PLA nanofabric as the radiative cooling layer (Fig. 9c), and semi-embedded AgNWs were fabricated as solar heating layer.[81]

Jung *et al.* proposed a Janus structure-based stretchable and breathable thermoelectric skin (Fig. 9d). The boron nitride–polydimethylsiloxane (BP) is used as radiative cooling layer and graphene nanoplatelet–polydimethylsiloxane nanofiber are developed as solar heating layer.[82] The boron nitride–polydimethylsiloxane generates the RC capability of $\Delta T_{cooling} = 4$ °C, and the high solar absorbance of the graphene nanoplatelet–polydimethylsiloxane nanofiber enables it to be photothermally heated. The flip-over able thermoelectric skin achieves a maximum power output of 5.73 μW cm^{-2} in passive radiative cooling mode, surpassing solar heating mode by 5.55 μW cm^{-2} in the morning. In the afternoon, it generates a maximum

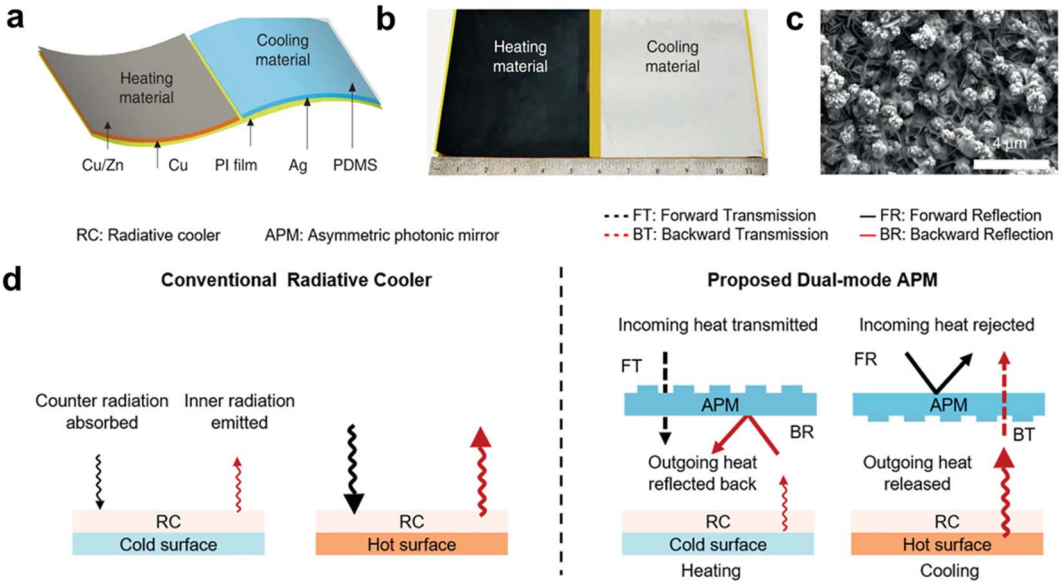

Fig. 8 (a) Structure of dual mode heating/cooling material. (b) Structure of dual mode heating/cooling material. (c) The photo of the dual mode material shows the different visible appearance of the heating/cooling parts. (d) SEM image of the heating material. (a–c) These figures have been adapted from ref. 77 with permission from Li, copyright 2020. (d) This figure has been adapted from ref. 78 with permission from Ly, copyright 2022.

power output of 18.59 μW cm^{-2} in solar heating mode, outperforming passive radiative cooling mode by 15.56 μW cm^{-2}.

In summary, a dual mode system, capability of either flipping or using rollers, typically incorporates a cooling layer structured similarly to traditional radiative cooling layers. This includes a series of materials, such as porous substances, textiles, photonic crystal structures, and the stacking of layers with different functionalities. For the solar heating side, materials are typically chosen based on their high solar absorption performance in 0.3 to 2.5 μm range to meet the requirement of raising the temperature of the object. Additionally, materials with low emissivity in the 8 to 13 μm range are preferred, such

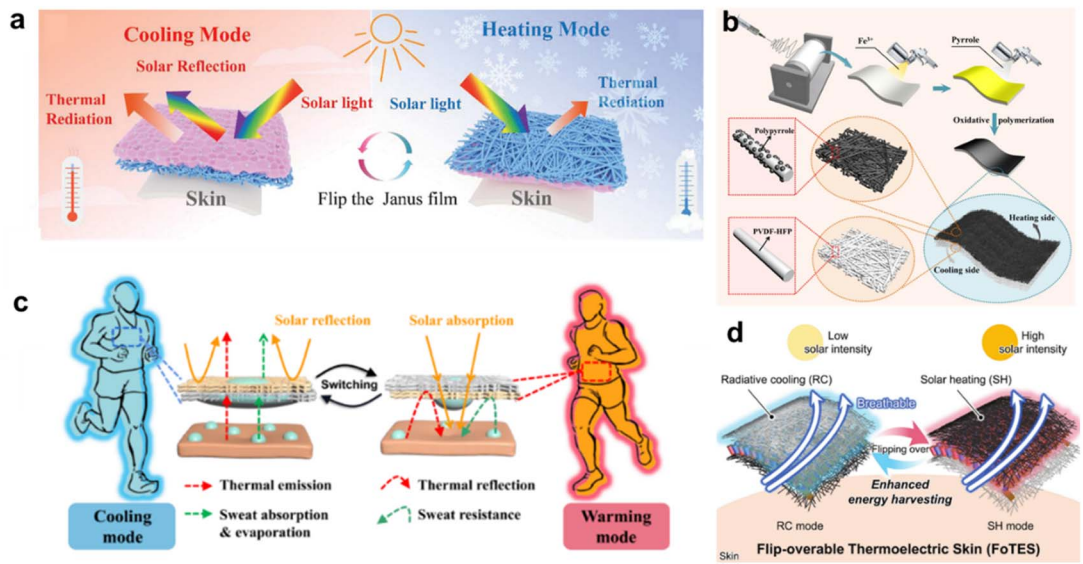

Fig. 9 (a) Cooling mode and heating mode. (b) Schematic of the fabrication procedure and microstructure of the dual mode fiber membrane. (c) Switchable thermal and sweat management principle. (d) Schematic illustration demonstrates the dual modes of RC and solar-heating modes which flip-overable thermoelectric skin switches from one mode to the other by flipping the device over. (a) This figure has been adapted from ref. 79 with permission from Yang, copyright 2023. (b) This figure has been adapted from ref. 80 with permission from Xiang, copyright 2022. (c) This figure has been adapted from ref. 81 with permission from Feng, copyright 2023. (d) This figure has been adapted from ref. 82 with permission from Jung, copyright 2023.

as MXene.[83–85] This choice maximizes the utilization of absorbed solar energy to raise the material's temperature. However, in practical applications, many materials with high solar absorption performance in 0.3 to 2.5 μm also exhibit relatively high emissivity in the 8 to 13 μm range. When served as the heating side, these materials can provide sub-ambient daytime cooling at the same time. Nevertheless, due to the high solar thermal conversion efficiency of such materials, the heating side in the dual mode system still maintains a temperature above ambient.[86] Examples of such materials include graphene,[87] carbon nanotubes, and carbon black. According to eqn (4), to achieve the temperature increase, the value of P_{net} needs to be less than 0. The ideal heating side requires higher absorption in 0.3 to 2.5 μm range, and lower emissivity in 8 to 13 μm range.

5.3 Temperature responsive dual mode system

The temperature-responsive materials are frequently utilized in both the realm of smart windows and the construction industry.[88] Thermochromic materials capitalize on solar heating to induce phase changes, thus rendering them cost-effective and energy-efficient due to their autonomy from a net energy input. Fundamentally, these materials undergo a transition stimulated by temperature, shifting from a state that allows sunlight to pass through to a state that blocks incident light and radiation, thereby hindering the transfer of energy between indoor and outdoor environments. Frequently, dual mode radiation cooling systems responsive to temperature employ materials sensitive to temperature, carefully orchestrating the spectral reflectance and absorption of the system. This orchestration facilitates the seamless transition between radiative cooling and radiative heating modes. Thermochromic materials, including liquid crystals,[89–91] perovskites,[92] ionic liquid gels,[93] and hydrogels,[94–97] have been utilized in solar modulation across the visible and near-infrared (NIR) spectrum. Temperature-responsive polymers most typically employed in the context of intelligent dual mode systems encompass thermosensitive hydrogels, shape memory materials, and phase-change substances.

5.3.1 Temperature responsive hydrogel. Temperature responsive hydrogels are commonly applied in smart windows.[98] Glass windows demand increased transparency, enhanced thermal conductivity, and decreased thickness. These hydrogels manifest transparency in cold weather and rapidly shift from transparency to semi-transparency or opacity in warmer conditions. pNIPAm stands as the prevailing hydrogel of choice.

Lin *et al.* transferred AgNWs onto the surface of pNIPAm to fabricate pNIPAm/AgNW composite materials.[99] At lower temperatures ($T < \tau_c$, phase transition temperature), pNIPAm cross-linked networks swell *via* intermolecular hydrophilic bonds, dispersing water molecules within the structure (Fig. 10a). The hydrogel's refractive index matches water's, ensuring solar transparency, while the AgNW mesh on top maintains high solar transmittance and thermal reflectance. Integrated in the thermal regulatory thermochromic (STR) window, it preserves these features at low temperatures. Beyond the τ_c, weakened hydrogen bonds disrupt water/pNIPAm links, prompting hydrophobic interactions and expelling water molecules (Fig. 10b). Chemical bonding confines pNIPAm's contraction to one side, inducing directional water transport and AgNW mesh accumulation. Phase separation creates polymer rich and poor microphases, scattering light, turning the hydrogel white, and efficiently reflecting sunlight. Additionally, a water layer (>0.1 mm) exhibits high thermal emissivity, reducing thermal reflection from the AgNW mesh, notably modulating thermal dynamics. The STR windows exhibit excellent solar modulation (58.4%) and thermal modulation (57.1%), demonstrating effective regulation of indoor temperatures during both daytime and nighttime.

Li *et al.* copolymerized *N*-isopropylacrylamide monomer (NIPAM) with 2-aminoethyl methacrylate (AEMA) monomer to synthesize a temperature-responsive hydrogel microparticle.[100] These resulting microparticles, comprising pNIPAm–AEMA or pNIPAm hydrogels, were injected between two glass slides to fabricate a thin-film hydrogel device. These microparticles manifest adjustable scattering characteristics, facilitating the simultaneous attainment of high-intensity transmission and comprehensive modulation of solar transmittance across a wide spectrum (Fig. 10c). Especially by tailoring the particle size and internal structure (Fig. 10d), the pNIPAm–AEMA hydrogel effectively extends light rejection into the IR region, contributing to a significantly enhanced infrared transmittance modulation of 75.6% and an ultra-high solar transmittance modulation of 81.3%.

Chen *et al.* conducted *in situ* free radical copolymerization of the hydrophilic monomer *N*,*N*-dimethylacrylamide (DMAA) with NIPAm at 25 °C,[24] resulting in the formation of a random copolymer, p(NIPAm-*co*-DMAA) (PND), within hydrogel matrices (Fig. 11a). Varying the DMAA content within the network allows for the modulation of the lower critical solution temperature. Below the τ_c, the hydrogel maintains transparency with a refractive index of 1.377, closely resembling that of water. As a result, the smart window exhibits exceptional transparency (Fig. 11b). Beyond the critical transition temperature, the PDMAA chains within the hydrogel network undergo collapse, forming hydrophobic and hydrophilic microdomains that induce light scattering. Consequently, the smart window transferred into a semi-transparent state. Notably, this material offers adjustable critical transition temperature and full-spectrum regulation, enabling adaptation to diverse climatic conditions for architectural thermal management. Moreover, the material can be fabricated into grid patterns and Chinese cut-paper designs using 3D printing techniques, affording dual effects of solar modulation and illumination control.

Mei *et al.* used PVDF films as top and bottom layers to encapsulate the pNIPAm hydrogel and improve the thermal emittance of the design.[101] The PVDF@pNIPAm film takes advantage of the synergistic impact of PVDF's high thermal emittance within the atmospheric transparency window (Fig. 11c), showcasing notable modulation of visible light (300 to 780 nm) reflectance/transmittance ($\Delta R_{vis} = 70.0\%$, $\Delta T_{vis} = 86.3\%$) and mid-infrared emissivity ($E_{LWIR} = 0.96$). This leads to

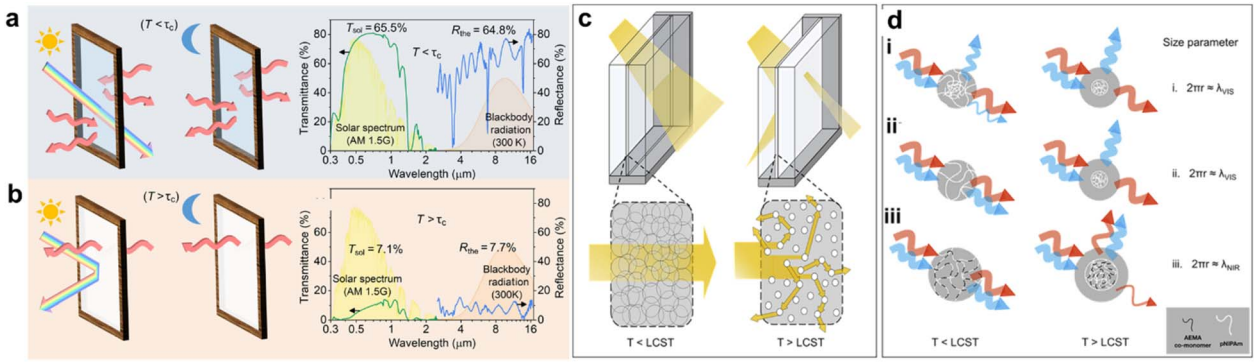

Fig. 10 (a) Schematic of optical performance in the cold condition and the corresponding spectrum. (b) Schematic of optical performance in the hot condition and the corresponding spectrum. (c) Schematic of transmittance modulation based on the tunable scattering behaviors of hydrogel particles. (d) Light manipulating with the aid of the phase transition of: (i) pNIPAm particles produced by one-pot synthesis; (ii) pNIPAm particles synthesized by continuous feeding method; (iii) pNIPAm–AEMA co-polymerized microparticles. Visible light and IR light are represented by blue and red arrows, respectively. (a and b) These figures have been adapted from ref. 99 with permission from Lin, copyright 2022. (c and d) These figures have been adapted from ref. 100 with permission from Li, copyright 2019.

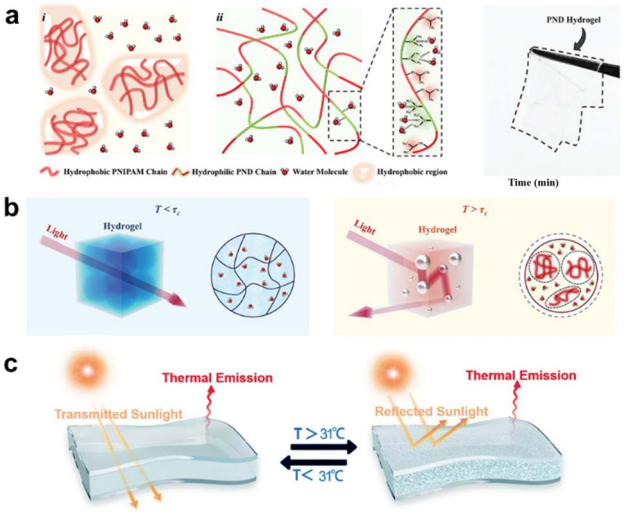

Fig. 11 (a) Schematic depiction of (i) PNIPAM and (ii) PND hydrogel structures. Right is the photograph of a transparent PND hydrogel. (b) Proposed thermochromic mechanism of PND hydrogel. (c) The sandwich structure film based on thermosensitive hydrogel, showing the intelligent regulation of the sunlight scattering. (a and b) These figures have been adapted from ref. 24 with permission from Chen, copyright 2023. (c) This figure has been adapted from ref. 101 with permission from Mei, copyright 2022.

sub-ambient radiative cooling of 1.8 to 3.7 °C during hot daylight hours and above-ambient heating of 4.3 to 5.8 °C during cold periods ($\Delta T_{\text{cooling–heating}} = 9.5$ °C) through reversible self-regulation.

5.3.2 Shape memory materials. Shape memory polymer (SMP) is a class of materials with the exceptional ability to return to a predefined initial shape upon exposure to external triggers, such as temperature or stress.[102–105] Applying this property to the realm of radiative cooling involves a prevalent approach where, under low-temperature conditions, the material is manipulated to induce an expanded surface area for the absorbent layer within composite materials. This enhancement results in increased absorption of solar energy, subsequently elevating the temperature. As the temperature rises, they undergo a phase transition, resulting in the restoration of their initial form. Employing these intelligent shape memory

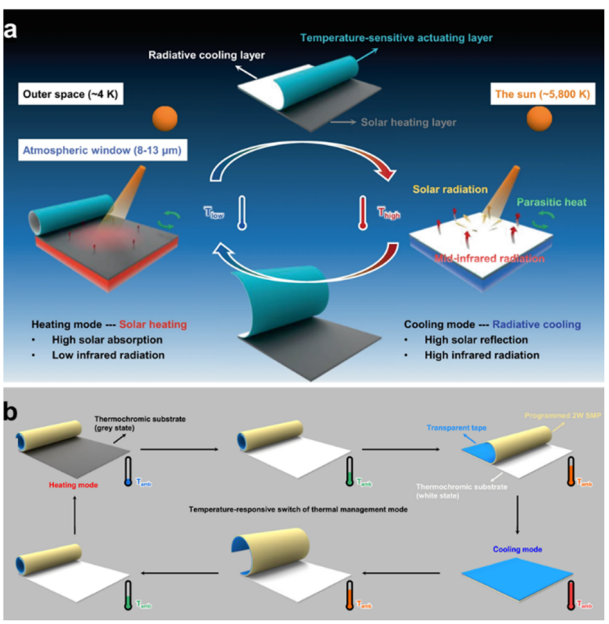

Fig. 12 (a) Schematic illustration of the dual mode radiative thermal management device switching between solar heating (left) and radiative cooling (right) with temperature. The dual mode device (top) consists of three functional layers: radiative cooling layer, temperature-sensitive actuating layer, and solar heating layer (not to scale). (b) The device consists of two main functional layers: a temperature-sensitive actuator with high-infrared emissivity composed of transparent tape and programmed 2W SMP and a thermochromic substrate with low-infrared emissivity. (a) This figure has been adapted from ref. 106 with permission from Zhang, copyright 2022. (b) This figure has been adapted from ref. 107 with permission from Zhang, copyright 2022.

materials facilitates temperature control during solar energy absorption and heat dissipation processes, enabling passive radiative cooling without the necessity of external energy input.

Zhang *et al.* demonstrated a high-performance, intelligent automatic-switching, and zero-energy-consumption dual mode radiative thermal management device.[106] This device comprises a radiative cooling layer (anatase TiO_2 nanoparticles encapsulated in DOP-modified PMP), a temperature-sensitive actuating layer (shape memory material), and a solar heating layer (aluminum plate with nano-sized chromium oxide powder) (Fig. 12a). When the temperature reaches the triggering temperature within the range of 23 to 24 °C, the SMP shrinks upon heating and expands upon cooling in the stretching direction, thereby controlling the opening and curling of the cooling and heating layers. The actuating layer exhibits excellent cyclic performance during repeated heating–cooling processes, indicating good long-term operational stability. By sensing temperature and spontaneously modulating its characteristics, the device achieves an average heating power of 859.8 W m^{-2} (approximately 91% of solar thermal conversion efficiency) in cold, and 126.0 W m^{-2} of average cooling power in hot, with no external energy consumption throughout the process. Compared to a copper plate, the temperature fluctuation is reduced by 21 K.

Inspired by the color change of Himalayan rabbit's hair and the folding–opening movement of *M. pudica*'s leaves,[107] the same research team devised a thermal management apparatus capable of autonomously and concurrently adjusting its spectral attributes across the solar and infrared wavelength spectrum. This innovative approach maximizes temperature control performance by harnessing both solar and outer space resources. The dual mode radiative thermal management device comprises three layers: a transparent adhesive tape with a 2W SMP film, a visible light thermochromic layer, and an infrared modulation layer (Fig. 12b). In contrast to earlier design, the notable feature of this design lies in integrating a visible light thermochromic layer as the intermediate stratum. This layer consists of a visible light thermochromic material capable of altering its color at varying temperatures. As the temperature of the heating plate increases, the visible light thermochromic layer undergoes a color change, effectively modulating the visible light emissivity. This unique ability enables the device to switch between heating mode ($R_{0.4–0.78\ \mu m}$ of 73% and $\varepsilon_{8–13\ \mu m}$ of 28%) and cooling mode ($R_{0.4–0.78\ \mu m}$ of 65% and $\varepsilon_{8–13\ \mu m}$ of 95%), rather than simply adjusting heating power or cooling power. The trigger temperature of the device is also adjustable to meet the demands in different application fields. Numerical prediction shows this device has the best effect of all-season energy saving for temperature control compared with the temperature responsive thermal-management devices in the literature.

Zhang *et al.* introduced the concept of utilizing shape memory materials as springs in the design of a switchable radiative cooler (SRC).[108] This innovative SRC consists of two key components: a radiative cooling coating and a temperature-responsive part (TRP). By harnessing the low thermal resistance state during hot weather conditions, the SRC efficiently transfers internal heat to the external radiative cooling coating for dissipation. However, when faced with colder weather, the SRC automatically transitions to a high thermal resistance state, effectively preventing the removal of indoor heat.

5.3.3 Phase change materials. In phase change materials, vanadium dioxide (VO_2) is one of the most representative thermochromic materials.[109] Its prominent metal-to-insulator transition occurs at a critical temperature τ_c of 340 K. At temperatures below τ_c, VO_2 is an insulator,[110,111] while upon heating to temperatures above τ_c, it becomes a metal, with its lattice structure transitioning from a monoclinic system to a rutile-type structure.

This process also involves a change in the band structure. When VO_2 becomes metallic, the 0.7 eV bandgap disappears, and the π overlap and d bands emerge, leading to a sudden change in the mid-infrared region from transparent to opaque. These characteristics enhance the application of VO_2 thin films in variable emissivity devices.[30,88]

Wang *et al.* utilized VO_2 in windows,[31] modulating the long-wave infrared (LWIR) emissivity (2.5 to 25 μm) and achieving perfect automatic switching between radiative cooling and solar heating. For this window, the NIR is blocked in summer to prevent solar heating while the visible transparency remains unchanged. In winter, both visible and NIR are transmitted while $\varepsilon_{LWIR,front}$ is switched to lower values, reducing radiative cooling heat loss (Fig. 13a). Here, authors kept $\varepsilon_{LWIR,back}$ low in both conditions to minimize the heat exchange between the indoors and outdoors.

This design reached a ΔT of 9.3% and a $\Delta\varepsilon_{LWIR}$ of 40%. The ε_{LWIR} performance of the smart window can be controlled by simply adjusting the spacer thickness and the VO_2 weight ratio, as well as doping. Furthermore, the fabricated scalable smart windows can provide different emissivity at high ($\varepsilon_{LWIR\text{-}H} = 0.61$) and low ($\varepsilon_{LWIR\text{-}L} = 0.21$) temperatures, thereby automatically regulating radiative cooling while maintaining luminous transparency and NIR modulation. In an overall building energy simulation, this radiative cooling thermochromic regulation window demonstrated higher heating and cooling energy savings in various climate zones compared to commercial low-emissivity glass, potentially reducing carbon emissions associated with heating and cooling and improving building sustainability. Moreover, this passive ε_{LWIR} control could be applied to a wide range of thermal regulation applications, including windows, walls, roofs, fabrics, and coatings.

Tang *et al.* developed the temperature-adaptive radiative coating based on the well-known metal–insulator transition of the strongly correlated electron materials $W_xV_{1-x}O_2$,[112] and the transition temperature (TMIT) is tailored to 22 °C by setting the composition x at 1.5%. They embedded a lithographically patterned two-dimensional array of thin $W_xV_{1-x}O_2$ blocks in a BaF_2 dielectric layer that sits on top of an Ag film (Fig. 13b). In the insulating state of $W_xV_{1-x}O_2$ at $T <$ TMIT, the material is largely transparent to the IR radiation in the 8 to 13 μm atmospheric window, so this atmospheric window is reflected by the Ag mirror with little absorption. By contrast, the $W_xV_{1-x}O_2$ becomes highly absorptive in the atmospheric window when it switches to the metallic state at $T >$ TMIT. The absorption is

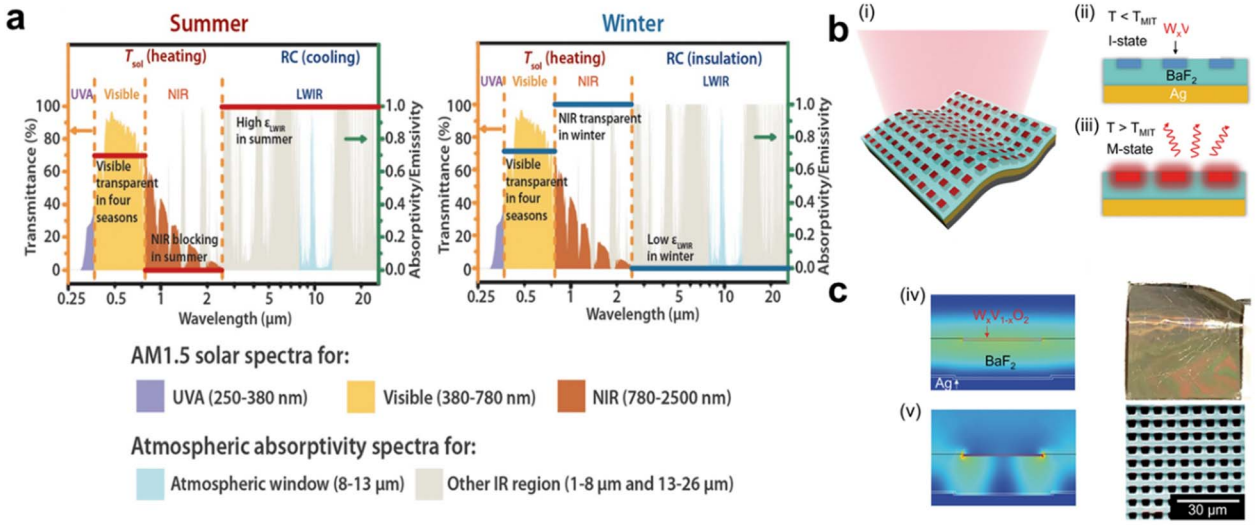

Fig. 13 (a) Concept of the ideal energy-saving smart window. The red and blue lines represent the spectra for an ideal energy-saving smart window in summer and winter. T_{sol} and thermal radiation in LWIR contribute to heating and cooling, respectively. Visible transparency remains constant. Windows should be NIR blocking and have high e_{LWIR} to promote radiative cooling in summer, and the response must be switched to the opposite in the winter. (b) Schematics of the structure (i), materials composition and working mechanism (ii and iii) of the TARC. Subpanels (iv) and (v) show the simulated distribution of electric field intensity below and above the transition temperature, respectively, when electromagnetic waves with a wavelength of 7.8 μm were normally incident on the TARC structure. (c) Photograph (2 cm × 2 cm) and false-color scanning electron microscope image of TARC showing high flexibility and structural consistency with the design. (a) This figure has been adapted from ref. 31 with permission from Wang, copyright 2021. (b and c) These figures have been adapted from ref. 112 with permission from Tang, copyright 2021.

further amplified by the designed photonic resonance with adjacent $W_xV_{1-x}O_2$ blocks as well as with the bottom Ag layer through the $\frac{1}{4}$-wavelength cavity (Fig. 13c). The $\frac{1}{4}$-wavelength cavity structure incorporates Fabry–Perot resonance and can be utilized to enhance thermal emission. In compliance with Kirchhoff's law of radiation, the emissivity of the sky window aligns with its absorptance, shifting from a lower magnitude to a higher one as the temperature surpasses TMIT. The fabricated temperature-adaptive radiative coating (TARC) optimally absorbs the solar energy and automatically switches thermal emittance from 0.20 for ambient temperatures lower than 15 °C to 0.90 for temperatures above 30 °C, driven by a photonically amplified metal–insulator transition.

5.4 Solution responsive dual mode system

Solution-stimulated responsive materials typically manifest as porous composites. Widely utilized solvents encompass water, ethanol, isopropanol, their mixtures or mineral oil. The fundamental principle underlying this concept is that in the absence of the solution, these materials exhibit a porous structure and inherent properties that result in higher solar reflectance and mid-infrared emissivity, thereby contributing to excellent radiative cooling performance. Upon immersion in the solution, the material transforms, transitioning to a transparent or semi-transparent state. This state change also leads to an alteration in the material's refractive index, enabling solar radiation to permeate the composite material and consequently induce heating of objects. This versatile approach holds practical appeal due to its scalability in real-world applications.

Mandal *et al.* have demonstrated the attainability of these optical dynamics through the reversible wetting of porous polymer coatings with fluids like alcohol or water.[113] In the solar wavelengths, reduction in optical scattering upon wetting changes of porous polymer coatings from reflective to transparent. For poly(vinylidene fluoride-*co*-hexafluoropropene) porous polymer coatings, this corresponds to solar and visible transmittance changes of up to 0.74 and 0.80, respectively (Fig. 14a and b). Furthermore, switchable sub-ambient radiative cooling (by 3.2 °C) and above-ambient solar heating (by 21.4 °C), color-neutral daylighting, and thermal camouflage are demonstrated.

Fei *et al.* fabricated a hierarchical porous coating from modified PVDF/cellulose acetate polymer networks.[114] It exhibits rapid switch between high solar reflection (96.6%) and high solar transmission (86.6%) (Fig. 14c). This results in 61.2 W m^{-2}-night time cooling power (cooling mode) and 720 W m^{-2} daytime heating power under typical tropical weather conditions (heating mode). Zhang *et al.* employed a porous SiO_2 coating that can be separated or merged with a refractive index-matched liquid (Fig. 14d).[115] This setup enables the adjustment of sunlight transmittance to achieve adaptive heating and cooling functions. This dual mode system facilitates a temperature rise of 10 °C during cold weather and a cooling effect of 5 °C in hot conditions. Shi *et al.* reported scalable fabrication of biosynthetic bacterial cellulose-based radiative cooling materials with switchable solar transmittance, which are developed by entangling silica microspheres with continuously secreted cellulose nanofibers during *in situ* cultivation (Fig. 14e and f).[116]

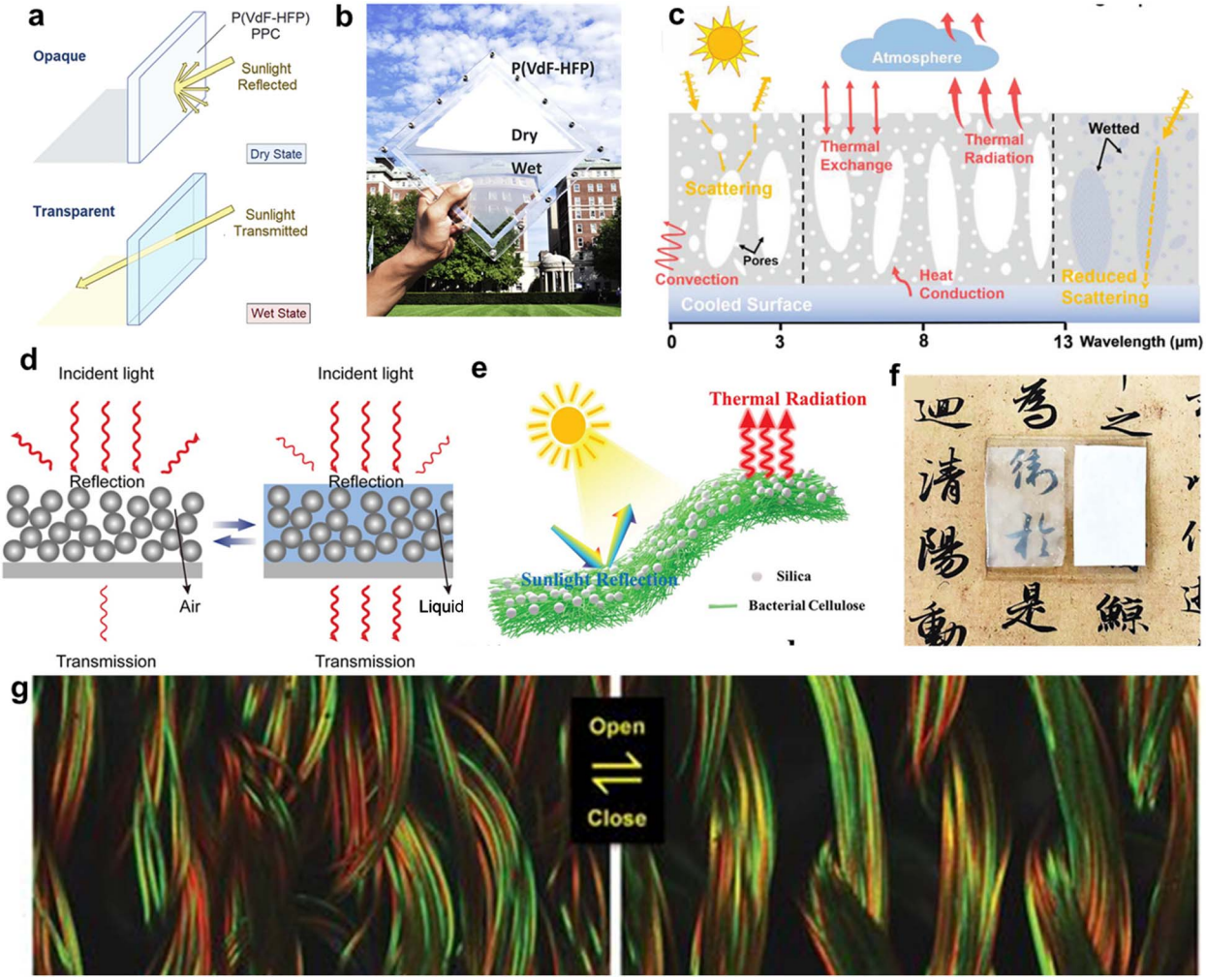

Fig. 14 (a) White to transparent switching of the porous P(VdF-HFP)-air/isopropanol system. (b) Photograph of the system showing dry and wet states. (c) Schematic illustration of working principle of designed hierarchical porous structure: passive radiative cooling mechanism including solar reflection and IR emission is shown along *x*-axis. (d) Mechanism of light transmission and reflection. (e) Schematic illustration of the radiative cooling mechanism of nanostructured Bio-RC films. (f) Photograph of nanostructured Bio-RC films in the transparent and opaque state. (g) Confocal fluorescent microscopy images showing the knitted fabric in the closed state (d) (low humidity) and the open state (e) (high humidity). Scale bars: 200 mm. (a and b) These figures have been adapted from ref. 113 with permission from Mandal, copyright 2019. (c) This figure has been adapted from ref. 114 with permission from Fei, copyright 2022. (d) This figure has been adapted from ref. 115 with permission from Zhang, copyright 2022. (e and f) These figures have been adapted from ref. 116 with permission from Zhang, copyright 2023. (g) This figure has been adapted from ref. 117 with permission from Zhang, copyright 2019.

The resulting film shows a high solar reflection (95.3%) that can be facilely switched between an opaque state and a transparent state upon wetting.

In the field of human thermal management, the body's perspiration process results in heightened local humidity levels. Furthermore, exercise can raise the body's surface temperature. Hence, both temperature and humidity stimuli can function as activating sources for a dual mode management system.

Zhang *et al.* utilized cellulose triacetate-based and polyethylene terephthalate fibers to fabricate dual-component fibers, subsequently coated with few-walled carbon nanotubes.[117] The obtained textile effectively modulated the infrared radiation by more than 35% as the relative humidity of the underlying skin changed. When subjected to heat and/or humidity, the yarns underwent collapse, causing the sub-elements of adjacent fibers to tightly intertwine, inducing resonant electromagnetic coupling. Conversely, in cold and/or dry conditions, the yarns exhibited an opposing response, thereby reducing heat dissipation (Fig. 14g). This facilitated effective gating of infrared radiation through the textile (*i.e.*, "opening" and "closing") in response to environmental changes. This infrared response was swift (<1 minute) and reversible. The researchers postulate that this infrared gating effect originates from an environment-adaptive electromagnetic coupling mechanism among carbon nanotubes coated fibers. Through humidity control, regulation of the fabric's infrared emissivity becomes feasible, allowing for dynamic manipulation of infrared radiation.

6. Summary and perspective

In summary, after the decade-long development, a state-of-the-art account of recent developments of smart materials for real-time on-demand intelligent radiative cooling and solar heating were provided. On demand stimuli materials have become one of the most promising approaches to fabricate switchable thermal-management devices to meet diverse requirements in different situations without any external energy consumption. For ideal solar heating, the materials should have high solar absorption (0.4 to 2.5 μm) and low infrared emission (2.5 to 15 μm). For ideal radiative cooling, the materials should reflect solar radiation as much as possible and strongly release heat by infrared radiation. However, an unavoidable challenge is that the environment and climate in the real world are dynamic. This requires that a zero-energy thermal-management device not only have the above two sets of electromagnetic spectrums but also be able to automatically switch them by spontaneously perceiving the change in the environment. Such a diverse responsive smart materials design strategy is a plausible approach for fabricating intelligent multi-modal systems. These dynamic dual mode thermal-management devices present great potential in the fields of thermal management, and smart devices. Despite the tremendous efforts made in developing novel dual mode strategies, many challenges remain while numerous opportunities exist in realizing on demand switch ability together with other intriguing functional properties. With the abovementioned requirements, future directions and potential solutions to existing challenges for dynamic dual mode thermal-management technology are proposed, as outlined below.

(1) Despite the considerable strides made, research into the practical applications of these materials remains in its infancy, with numerous challenges yet to be surmounted on the path to commercialization. To begin with, the implementation of electrically stimulated smart materials often necessitates the assembly of electrochromic devices for modulation, leading to a relatively intricate fabrication process. Future research should be directed toward enhancing the process's scalability, building upon established packaging methodologies, and elevating the electrochromic performance. The scalability of mechanically induced stimuli is constrained by the uncertain and intricate control of stimulation sources, thereby rendering its expansibility rather limited. Consequently, forthcoming studies should focus on formulating strategies to augment precision while heightening scalability. As for thermochromic materials, their current modulations primarily revolve around adjusting temperature to manipulate infrared emissivity, predominantly catering to smart window applications. Hence, forthcoming investigations should strive to develop more precise and controlled modulation methods, concurrently expanding their potential application domains. While solution-responsive materials boast affordability and ease of scalability, the manageability of their operational procedures is yet to be refined. Furthermore, humidity-responsive materials exhibit enhanced compatibility compared to their counterparts. In future research, consideration may be given to the redesign of structures, integrating these humidity-responsive materials with other smart constituents to facilitate multifaceted thermal radiation modulation, thus accommodating intricate requirements.

(2) In the foreseeable future, a multitude of cutting-edge stimulus-responsive materials is expected to emerge, showcasing their rapid adaptability in modulating thermal radiation characteristics in response to dynamic changes in the external environment. This forefront material innovation is poised to significantly amplify the performance and efficacy of dual mode systems.

(3) The continuous advancement of technology may propel the application of stimulus-responsive smart radiative cooling and solar heating dual mode systems into broader domains, such as aerospace, agriculture, healthcare, and beyond.

(4) As dual-mode radiative cooling and solar heating systems continue to witness expanding applications across diverse fields, it becomes imperative to delineate standardized evaluation criteria tailored to the specific domains of application. For example, in the realm of smart windows, the establishment of uniform application standards for dual-mode systems is of paramount importance. This entails the adoption of consistent performance metrics to facilitate comprehensive performance comparisons. Outdoor experimentation, conducted under controlled environmental conditions, serves as a rigorous methodology for evaluating critical aspects such as radiative cooling, solar heating, and UV resistance capabilities.

(5) In terms of cooling and heating performance, an ideal dual mode system requires meaningful daytime radiative cooling layer and high efficiency solar heating layer. Nevertheless, various stimulus systems inherently possess their own limitations. For the cooling side, most of them cannot achieve a solar reflectance exceeding 94%. Especially for electrical, temperature responsive and solution responsive dual mode systems. Mechanically responsive dual mode systems may offer a more feasible approach to fulfilling this ideal requirement, especially when applied to Janus films and textiles.[80,81,84] Hence, developing meaningful daytime radiative cooling layer is necessary. Additionally, for the heating side, it is important to consider self-cleaning, superhydrophobic properties, as well as higher solar absorptivity and lower emissivity in the 8–13 μm range.

Conflicts of interest

The authors declare no conflicts of interest.

Acknowledgements

The authors express sincere thanks to members of the EMSL lab for useful discussion of the research.

Notes and references

1 A. K. Jain, *Nat. Food*, 2023, **4**, 139–140.
2 P. In Hong, Y. Sang Wook, C. Wenju, W. Guojian, M. Seung Ki and L. Sang Ki, *Nat. Clim. Change*, 2023, **13**, 816–822.

3 B. Tao, J. Gensuo and X. Xiyan, *Nat. Clim. Change*, 2023, 462–469.
4 J. Song, Y. Wang and J. Tang, *Sci. Rep.*, 2016, **6**, 33315.
5 Y. Zhao, Z. Li, C. Deger, M. Wang, M. Peric, Y. Yin, D. Meng, W. Yang, X. Wang, Q. Xing, B. Chang, E. G. Scott, Y. Zhou, E. Zhang, R. Zheng, J. Bian, Y. Shi, I. Yavuz, K.-H. Wei, K. N. Houk and Y. Yang, *Nat. Sustain.*, 2023, **6**, 539–548.
6 M. Luqman and T. Al-Ansari, *Energy Convers. Manage.*, 2021, **244**, 114525.
7 G. Fekadu and S. Subudhi, *Renewable Sustainable Energy Rev.*, 2018, **93**, 364–379.
8 Y. Peng and Y. Cui, *Joule*, 2020, **4**, 724–742.
9 M. Lee, G. Kim, Y. Jung, K. R. Pyun, J. Lee, B.-W. Kim and S. H. Ko, *Light: Sci. Appl.*, 2023, **12**, 134.
10 Z. Wang, S. K. Kim and R. Hu, *Matter*, 2022, **5**, 780–782.
11 L. Tang, B. Lyu, D. Gao, Z. Jia and J. Ma, *Chem. Eng. J.*, 2023, **465**, 142829.
12 K. K. Bertine and E. D. Goldberg, *Science*, 1971, **173**, 233–235.
13 C. W. Garrett, *Prog. Energy Combust. Sci.*, 1992, **18**, 369–407.
14 F. P. Perera, *Environ. Health Perspect.*, 2016, **125**, 141–148.
15 M. C. Huang, M. Yang, X. J. Guo, C. H. Xue, H. D. Wang, C. Q. Ma, Z. Bai, X. Zhou, Z. Wang, B. Y. Liu, Y. G. Wu, C. W. Qiu, C. Hou and G. Tao, *Prog. Mater. Sci.*, 2023, **137**, 101144.
16 W. Su, P. Cai, J. Darkwa, M. Hu, G. Kokogiannakis, C. Xu and L. Wang, *Appl. Therm. Eng.*, 2023, **235**, 121305.
17 J. Liang, J. Wu, J. Guo, H. Li, X. Zhou, S. Liang, C.-W. Qiu and G. Tao, *Natl. Sci. Rev.*, 2023, **10**, nwac208.
18 S. Basu, K. S. Hariharan, S. M. Kolake, T. Song, D. K. Sohn and T. Yeo, *Appl. Energy*, 2016, **18**, 1–13.
19 Z. Qian, Y. Li and Z. Rao, *Energy Convers. Manage.*, 2016, **126**, 622–631.
20 W. Zichen and D. Changqing, *Renewable Sustainable Energy Rev.*, 2021, **139**, 110685.
21 Z. Fang, L. Ding, L. Li, K. Shuai, B. Cao, Y. Zhong, Z. Meng and Z. Xia, *ACS Photonics*, 2021, **8**, 2781–2790.
22 Y. Wu, B. Liu, R. Zhang, T. Yu, M. Pu, X. Li, X. Ma, Y. Guo and X. Luo, *Energy Build.*, 2023, **296**, 113423.
23 S. Z. Sheng, J. L. Wang, B. Zhao, Z. He, X. F. Feng, Q. G. Shang, C. Chen, G. Pei, J. Zhou, J. W. Liu and S. H. Yu, *Nat. Commun.*, 2023, **14**, 3231.
24 G. Chen, K. Wang, J. Yang, J. Huang, Z. Chen, J. Zheng, J. Wang, H. Yang, S. Li, Y. Miao, W. Wang, N. Zhu, X. Jiang, Y. Chen and J. Fu, *Adv. Mater.*, 2023, e2211716.
25 X. Ao, B. Li, B. Zhao, M. Hu, H. Ren, H. Yang, J. Liu, J. Cao, J. Feng, Y. Yang, Z. Qi, L. Li, C. Zou and G. Pei, *Proc. Natl. Acad. Sci. U. S. A.*, 2022, **119**, e2120557119.
26 X. Xue, M. Qiu, Y. Li, Q. M. Zhang, S. Li, Z. Yang, C. Feng, W. Zhang, J. G. Dai, D. Lei, W. Jin, L. Xu, T. Zhang, J. Qin, H. Wang and S. Fan, *Adv. Mater.*, 2020, **32**, 1906751.
27 J. Mandal, Y. Yang, N. Yu and A. P. Raman, *Joule*, 2020, **4**, 1350–1356.
28 A. Pirvaram, N. Talebzadeh, S. N. Leung and P. G. O'Brien, *Renewable Sustainable Energy Rev.*, 2022, **162**, 112415.
29 Y. Jin, Y. Jeong and K. Yu, *Adv. Funct. Mater.*, 2022, **33**, 2207940.
30 R. Zhang, R. Z. Li, P. Xu, W. H. Zhong, Y. F. Zhang, Z. Y. Luo and B. Xiang, *Chem. Eng. J.*, 2023, **471**, 144527.
31 S. Wang, T. Jiang, Y. Meng, R. Yang, G. Tan and Y. Long, *Science*, 2021, **374**, 1501–1504.
32 S. Ahmed, S. Li, Z. Li, G. Xiao and T. Ma, *Appl. Energy*, 2022, **308**, 118363.
33 L. Zhu, A. Raman, K. X. Wang, M. A. Anoma and S. Fan, *Optica*, 2014, **191**, 662–668.
34 B. Zhao, K. Lu, M. Hu, J. Liu, L. Wu, C. Xu, Q. Xuan and G. Pei, *Renewable Energy*, 2022, **191**, 662–668.
35 M. Li, Z. Yan and D. Fan, *ACS Appl. Mater. Interfaces*, 2023, **15**, 17848–17857.
36 Z. Yan, H. Zhai, D. Fan and Q. Li, *Nano Today*, 2023, **51**, 101897.
37 K. Li, M. Li, C. Lin, G. Liu, Y. Li and B. Huang, *Small*, 2023, **19**, 2206149.
38 J. Liu, J. Zhang, H. Tang, Z. Zhou, D. Zhang, L. Ye and D. Zhao, *Nano Energy*, 2020, **81**, 105611.
39 Y. Zhang, W. Zhu, C. Zhang, J. Peoples, X. Li, A. L. Felicelli, X. Shan, D. M. Warsinger, T. Borca-Tasciuc, X. Ruan and T. Li, *Nano Lett.*, 2022, **22**, 2618–2626.
40 I. Haechler, H. Park, G. Schnoering, T. Gulich, M. Rohner, A. Tripathy, A. Milionis, T. M. Schutzius and D. Poulikakos, *Sci. Adv.*, 2021, **7**, 3978.
41 M. Liao, D. Banerjee, T. Hallberg, C. Akerlind, M. M. Alam, Q. Zhang, H. Kariis, D. Zhao and M. P. Jonsson, *Adv. Sci.*, 2023, **10**, 2206510.
42 S. Y. Heo, D. H. Kim, Y. M. Song and G. J. Lee, *Adv. Energy Mater.*, 2021, **12**, 2103258.
43 W. Z. Song, X. X. Wang, H. J. Qiu, N. Wang, M. Yu, Z. Y. Fan, S. Ramakrishna, H. Hu and Y. Z. Long, *Nano Energy*, 2021, **82**, 105695.
44 M. Hu, B. Zhao, X. Ao, n. Suhendri, J. Cao, Q. Wang, S. Riffat, Y. Su and G. Pei, *Energy Convers. Manage.*, 2021, **236**, 114057.
45 C. Chen, R. Wang, X. L. Li, B. Zhao, H. Wang, Z. Zhou, J. Zhu and J. W. Liu, *Nano Lett.*, 2022, **22**, 4131–4136.
46 J. Wang, G. Tan, R. Yang and D. Zhao, *Cell Rep. Phys. Sci.*, 2022, **3**, 101198.
47 Y. An, Y. Fu, J. G. Dai, X. Yin and D. Lei, *Cell Rep. Phys. Sci.*, 2022, **3**, 101098.
48 X. Li, S. Shao, M. Huang, S. Zhang and W. Guo, *iScience*, 2023, **26**, 105894.
49 B. Xie, Y. Liu, W. Xi and R. Hu, *Mater. Today Energy*, 2023, **34**, 101302.
50 C. H. Xue, R. X. Wei, X. J. Guo, B. Y. Liu, M. M. Du, M. C. Huang, H. G. Li and S. T. Jia, *Compos. Sci. Technol.*, 2022, **220**, 109279.
51 A. P. Raman, M. Abou Anoma, L. Zhu, E. Rephaeli and S. Fan, *Nature*, 2014, **515**, 540–544.
52 X. Meng, Z. Chen, C. Qian, Z. Song, L. Wang, Q. Li and X. Chen, *ACS Appl. Mater. Interfaces*, 2022, **15**, 2256–2266.
53 T. Lauster, A. Mauel, K. Herrmann, V. Veitengruber, Q. Song, J. Senker and M. Retsch, *Adv. Sci.*, 2023, **10**, e2206616.
54 G. J. Lee, Y. J. Kim, H. M. Kim, Y. J. Yoo and Y. M. Song, *Adv. Opt. Mater.*, 2018, **6**, 1800707.

55 J. P. Bijarniya, J. Sarkar and P. Maiti, *Renewable Sustainable Energy Rev.*, 2020, **133**, 110263.
56 B. Zhao, M. Hu, X. Ao, N. Chen and G. Pei, *Appl. Energy*, 2018, **236**, 489–513.
57 H. Zhang, C. S. Ly Kally, X. Liu, Z. Chen, M. Yan, Z. Wu, X. Wang, Y. Zheng, H. Zhou and T. Fan, *Proc. Natl. Acad. Sci. U.S.A.*, 2020, **117**, 14657–14666.
58 S. Y. Heo, G. J. Lee and Y. M. Song, *J. Mater. Chem. C*, 2022, **10**, 9915–9937.
59 M. M. Hossain and M. Gu, *Adv. Sci.*, 2016, **3**, 1500360.
60 H. Gong, W. Li, G. Fu, Q. Zhang, J. Liu, Y. Jin and H. Wang, *J. Mater. Chem. A*, 2022, **10**, 6269–6290.
61 J. T. S. Allan, S. Quaranta, I. I. Ebralidze, J. G. Egan, J. Poisson, N. O. Laschuk, F. Gaspari, E. B. Easton and O. V. Zenkina, *ACS Appl. Mater. Interfaces*, 2017, **9**, 40438–40445.
62 J. Chen, G. Song, S. Cong and Z. Zhao, *Adv. Mater.*, 2023, e2300179.
63 G. Cai, J. Wang and P. S. Lee, *Acc. Chem. Res.*, 2016, **49**, 1469–1476.
64 P. Yang, P. Sun and W. Mai, *Mater. Today*, 2016, **19**, 394–402.
65 X. Zhang, Y. Tian, W. Li, S. Dou, L. Wang, H. Qu, J. Zhao and Y. Li, *Sol. Energy Mater. Sol. Cells*, 2019, **200**, 109916.
66 H. Zheng, J. Z. Ou, M. S. Strano, R. B. Kaner, A. Mitchell and K. Kalantar-zadeh, *Adv. Funct. Mater.*, 2011, **21**, 2175–2196.
67 J. Mandal, S. Du, M. Dontigny, K. Zaghib, N. Yu and Y. Yang, *Adv. Funct. Mater.*, 2018, **28**, 1802180.
68 M. Y. Li, D. Q. Liu, H. F. Cheng, L. Peng and M. Zu, *Sci. Adv.*, 2020, **6**, eaba3494.
69 Y. F. Rao, J. Y. Dai, C. X. Sui, Y. T. Lai, Z. Li, H. M. Fang, X. Q. Li, W. Li and P. C. Hsu, *ACS Energy Lett.*, 2021, **6**, 3906–3915.
70 Y. Deng, Y. Yang, Y. Xiao, H. L. Xie, R. Lan, L. Zhang and H. Yang, *Adv. Funct. Mater.*, 2023, **33**, 2301319.
71 D. Cho, Y. S. Shim, J. W. Jung, S. H. Nam, S. Min, S. E. Lee, Y. Ham, K. Lee, J. Park, J. Shin, J. W. Hong and S. Jeon, *Adv. Sci.*, 2020, **7**, 1903708.
72 H. Zhao, Q. Sun, J. Zhou, X. Deng and J. Cui, *Adv. Mater.*, 2020, **32**, e2000870.
73 X. Li, Z. Ding, G. E. Lio, J. Zhao, H. Xu, L. Pattelli, L. Pan and Y. Li, *Chem. Eng. J.*, 2023, **461**, 142095.
74 Z. Zhou, Y. Fang, X. Wang, E. Yang, R. Liu, X. Zhou, Z. Huang, H. Yin, J. Zhou and B. Hu, *Nano Energy*, 2022, **93**, 106865.
75 S. Wang, Y. Dong, Y. Li, K. Ryu, Z. Dong, J. Chen, Z. Dai, Y. Ke, J. Yin and Y. Long, *Mater. Horiz.*, 2023, **10**, 4243–4250.
76 Q. Chen, Y. Lu, J. Zhang, D. Li, T. Huang, C. Lou, M. Zhao, W. Song and H. Xu, *Nano Energy*, 2023, **114**, 108610.
77 X. Li, B. Sun, C. Sui, A. Nandi, H. Fang, Y. Peng, G. Tan and P.-C. Hsu, *Nat. Commun.*, 2020, **11**, 6101.
78 K. C. S. Ly, X. Liu, X. Song, C. Xiao, P. Wang, H. Zhou and T. Fan, *Adv. Funct. Mater.*, 2022, **32**, 2203789.
79 P. Yang, J. He, Y. Ju, Q. Zhang, Y. Wu, Z. Xia, L. Chen and S. Tang, *Adv. Sci.*, 2023, **10**, e2206176.
80 B. Xiang, R. Zhang, X. Zeng, Y. Luo and Z. Luo, *Adv. Fiber Mater.*, 2022, **4**, 1058–1068.
81 S. Feng, L. Yao, X. Chen, C. Liu, X. Bu, Y. Huang, M. He and Y. Zhou, *J. Colloid Interface Sci.*, 2023, **648**, 117–128.
82 Y. Jung, S. Jeong, J. Ahn, J. Lee and S. H. Ko, *Small*, 2023, 2304338.
83 M. Shi, M. Shen, X. Guo, X. Jin, Y. Cao, Y. Yang, W. Wang and J. Wang, *ACS Nano*, 2021, **15**, 11396–11405.
84 M. Shi, Z. Song, J. Ni, X. Du, Y. Cao, Y. Yang, W. Wang and J. Wang, *ACS Nano*, 2023, **17**, 2029–2038.
85 N. Selvakumar, G. Karthik, S. Jayaraj and H. C. Barshilia, *Sol. Energy Mater. Sol. Cells*, 2021, **221**, 110906.
86 J. H. Wang, C. H. Xue, B. Y. Liu, X. J. Guo, L. C. Hu, H. D. Wang and F. Q. Deng, *ACS Omega*, 2022, **7**, 15247–15257.
87 Z. Luo, B. X. Li, H. Sun, J. Liu, H. Y. Zhao, Z. Z. Yu and D. Yang, *J. Mater. Chem. A*, 2023, **11**, 16595–16604.
88 M. Liu, X. Li, L. Li, L. Li, S. Zhao, K. Lu, K. Chen, J. Zhu, T. Zhou, C. Hu, Z. Lin, C. Xu, B. Zhao, G. Zhang, G. Pei and C. Zou, *ACS Nano*, 2023, **17**, 9501–9509.
89 Y. K. Kim, X. Wang, P. Mondkar, E. Bukusoglu and N. L. Abbott, *Nature*, 2018, **557**, 539–544.
90 Z. Zhang, X. Yang, Y. Zhao, F. Ye and L. Shang, *Adv. Mater.*, 2023, **35**, 2300220.
91 J. Uchida, B. Soberats, M. Gupta and T. Kato, *Adv. Mater.*, 2022, **34**, 2109063.
92 L. N. Quan, F. P. García de Arquer, R. P. Sabatini and E. H. Sargent, *Adv. Mater.*, 2018, **30**, 1801996.
93 T. P. Lodge and T. Ueki, *Acc. Chem. Res.*, 2016, **49**, 2107–2114.
94 W. Cheng, X. Wu, Y. Zhang, D. Wu, L. Meng, Y. Chen and X. Tang, *Trends Food Sci. Technol.*, 2022, **129**, 244–257.
95 H. Yuk, B. Lu and X. Zhao, *Chem. Soc. Rev.*, 2018, **48**, 642–1667.
96 S. Li, S. Dong, W. Xu, S. Tu, L. Yan, C. Zhao, J. Ding and X. Chen, *Adv. Sci.*, 2018, **5**, 1700527.
97 X. Yao, J. Liu, C. Yang, X. Yang, J. Wei, Y. Xia, X. Gong and Z. Suo, *Adv. Mater.*, 2019, **31**, 1903062.
98 K. Wang, L. Zhang and X. Jiang, *J. Colloid Interface Sci.*, 2023, **652**, 663–672.
99 C. Lin, J. Hur, C. Y. H. Chao, G. Liu, S. Yao, W. Li and B. Huang, *Sci. Adv.*, 2022, **8**, eabn7359.
100 X. H. Li, C. Liu, S. P. Feng and N. X. Fang, *Joule*, 2019, **3**, 290–302.
101 X. Mei, T. Wang, M. Chen and L. Wu, *J. Mater. Chem. A*, 2022, **10**, 11092–11100.
102 Y. Xia, Y. He, F. Zhang, Y. Liu and J. Leng, *Adv. Mater.*, 2020, **33**, 2000713.
103 W. M. Huang, Z. Ding, C. C. Wang, J. Wei, Y. Zhao and H. Purnawali, *Mater. Today*, 2010, **13**, 54–61.
104 J. G. Hardy, M. Palma, S. J. Wind and M. J. Biggs, *Adv. Mater.*, 2016, **28**, 5717–5724.
105 M. S. Kim, J. K. Heo, H. Rodrigue, H. T. Lee, S. Pané, M. W. Han and S. H. Ahn, *Adv. Mater.*, 2023, **35**, 2208517.
106 Q. Zhang, Y. Lv, Y. Wang, S. Yu, C. Li, R. Ma and Y. Chen, *Nat. Commun.*, 2022, **13**, 4874.
107 Q. Zhang, Y. Wang, Y. Lv, S. Yu and R. Ma, *Proc. Natl. Acad. Sci. U. S. A.*, 2022, **119**, e2207353119.

108 H. Zhang, J. Huang and D. Fan, *ACS Appl. Energy Mater.*, 2022, **5**, 6003–6010.
109 T. Chang, Y. Zhu, C. Cao, C. Yang, H. Luo, P. Jin and X. Cao, *Acc. Mater. Res.*, 2021, **2**, 714–725.
110 K. Liu, S. Lee, S. Yang, O. Delaire and J. Wu, *Mater. Today*, 2018, **21**, 875–896.
111 Y. Chen, S. Zhang, F. Ke, C. Ko, S. Lee, K. Liu, B. Chen, J. W. Ager, R. Jeanloz, V. Eyert and J. Wu, *Nano Lett.*, 2017, **17**, 2512–2516.
112 K. C. Tang, K. C. Dong, J. C. Li, M. P. Gordon, F. G. Reichertz, H. Kim, Y. Rho, Q. J. Wang, C. Y. Lin, C. P. Grigoropoulos, A. Javey, J. J. Urban, J. Yao, R. Levinson and J. Q. Wu, *Science*, 2021, **374**, 1504–1509.
113 J. Mandal, M. Jia, A. Overvig, Y. Fu, E. Che, N. Yu and Y. Yang, *Joule*, 2019, **3**, 3088–3099.
114 J. Fei, D. Han, J. Ge, X. Wang, S. W. Koh, S. Gao, Z. Sun, M. P. Wan, B. F. Ng, L. Cai and H. Li, *Adv. Funct. Mater.*, 2022, **32**, 2203582.
115 C. Zhang, J. Yang, Y. Li, J. Song, J. Guo, Y. Fang, X. Yang, Q. Yang, D. Wang and X. Deng, *Adv. Funct. Mater.*, 2022, **32**, 2208144.
116 S. Shi, P. Lv, C. Valenzuela, B. Li, Y. Liu, L. Wang and W. Feng, *Small*, 2023, 2301957.
117 X. A. Zhang, S. Yu, B. Xu, M. Li, Z. Peng, Y. Wang, S. Deng, X. Wu, Z. Wu, M. Ouyang and Y. H. Wang, *Science*, 2019, **363**, 619–623.